

High-resolution spectroscopy of Pr³⁺ions in YAl₃(BO₃)₄:Pr³⁺. Crystal-field, hyperfine, and electron-deformation interactions

B. Z. Malkin¹, T. A. Igolkina^{2,3}, K. N. Boldyrev⁴, A. Baraldi⁵, E. P. Chukalina², M. N. Popova^{2,*}

¹ Kazan Federal University, Kazan 420008, Russia

² Institute of Spectroscopy, Russian Academy of Sciences, Troitsk, Moscow 108840, Russia

³ Moscow Institute of Physics and Technology (National Research University), Dolgoprudnyi, Moscow region 141700, Russia

⁴ Beijing Institute of Technology (BIT), Zhuhai BIT, Zhuhai 519088, P. R. China

⁵ Dept. of Mathematical, Physical and Computer Sciences, University of Parma, Parma 43124, Italy

Abstract

Optical transmission spectra of YAl₃(BO₃)₄ crystals doped with the Pr³⁺ ions in concentrations 1 and 2.5 at. % were studied by high-resolution (up to 0.05 cm⁻¹) Fourier spectroscopy, including in magnetic field parallel to the trigonal *c* axis of the crystal. The *g* factors of several crystal-field doublets of Pr³⁺ were determined. The crystal-field calculations performed using the exchange-charge model and high-resolution spectroscopy data allowed us to obtain a physically reasonable set of crystal-field parameters. The observed splitting of a number of doublets in zero magnetic field is explained by the presence of random lattice deformations. Simulation of the profiles of observed deformational doublets was carried out taking into account both hyperfine and electron-deformation interactions. The width of the distribution function of random strains was estimated. The main sources of random strains in YAl₃(BO₃)₄:Pr³⁺ crystals are discussed.

Keywords: YAl₃(BO₃)₄:Pr³⁺, high-resolution Fourier spectroscopy, Zeeman splitting, crystal-field calculations, crystal-field parameters, deformation splitting, simulation of line profiles

* corresponding author, e-mail: popova@isan.troitsk.ru

I. INTRODUCTION

Yttrium aluminum borate $\text{YAl}_3(\text{BO}_3)_4$ (YAB) is a multifunctional material with attractive physical and chemical properties. It is characterized by mechanical, chemical and thermal stability [1], uniquely high thermal conductivity [2], transparency in a wide spectral range, and high nonlinear optical coefficient [3], [4]. Using a 2.94 mm thick YAB crystal, 240 kW peak power at 266 nm (the fourth harmonic of a Nd:YAG laser) was achieved [3]. Doped with rare-earth (RE) ions, YAB crystals are used as nonlinear active media for self-frequency-doubling and self-frequency-summing lasers (see, e.g., [5-8]). YAB crystallizes in the *R*32 noncentrosymmetric space symmetry group and belongs to the family of compounds with the structure of the natural mineral huntite [9]. RE³⁺ ions substitute for Y³⁺ ions and reside in isolated REO₆ distorted prisms with *D*₃ point symmetry group, which do not share oxygen atoms with other REO₆ units. Such structural feature results in a low concentration quenching of RE luminescence [10,11]; as a consequence, YAB crystals with high concentration of RE ions are used as active media for microchip lasers [12-15]. Concentrated REAl₃(BO₃)₄ crystals are multiferroics [16-19], in particular, a giant magnetoelectric effect was demonstrated on HoAl₃(BO₃)₄ [17]. It has been shown that magnetoelectric properties of REAl₃(BO₃)₄ crystals can be well described using crystal-field parameters obtained from spectroscopic data [19]. YAB:RE³⁺ crystals are efficient phosphors [20-22], they can be used, in particular, for temperature sensing [23].

Luminescence of praseodymium ions Pr³⁺ imbedded into a crystal or glass is effectively employed in modern optical technologies. Such crystals are used as phosphors [24-27] and laser media [28-32]. Ultra-sensitive low-temperature luminescent thermometry based on Boltzmann behavior of the crystal-field levels of Pr³⁺ was recently demonstrated with CaNb₂O₆:Pr³⁺ [33]. Pr³⁺-doped crystals are considered for applications in quantum informatics devices [34-40]. The long coherence times of hyperfine structure levels required in this case have been recorded for Pr³⁺ in oxide crystals Y₂SiO₅ [36-39] and La₂(WO₄)₃ [40].

The above justifies the interest in studying the crystal-field and hyperfine structure of the praseodymium levels in YAB:Pr³⁺ crystal. A recent high-resolution study of the temperature-dependent polarized absorption spectra of YAB:Pr³⁺ (1 at. %) crystals [41] allowed us to specify the energies of CF levels, the previous information on which was incomplete or contradictory [42,43], and to reveal deformation splittings of spectral lines corresponding to optical transitions between singlet and doublet CF levels. Here, we add a new experimental information on magnetic *g* factors and deformation splittings for Pr³⁺ doped into YAB crystals at concentrations of 1 at. % and 2.5 at. % and grown with different fluxes, and we simulate the spectral line shape based on CF calculations, taking into account both hyperfine and electron-deformation interactions.

II. EXPERIMENTAL DETAILS

In addition to the YAB:Pr³⁺(1 at. %) crystal grown at the L.V. Kirenskii Institute of Physics in Krasnoyarsk using the solution-melt method with the Bi₂Mo₃O₁₂-based flux [44] and studied in [41], a YAB:Pr³⁺(2.5 at. %) crystal grown at the Moscow State University by N.I. Leonyuk using the same method but with the K₂Mo₃O₁₀-based flux [9] was studied. Also, the deformation splittings in the absorption spectra of a YAB:Pr³⁺(1 at. %) crystal grown with the K₂O/MoO₃/B₂O₃ mixed flux at the University of Parma [43] were analysed.

Transmission spectra in the range of 2000–23,000 cm^{−1} were recorded on a Bruker IFS 125 HR Fourier spectrometer. Measurements were performed in the temperature range of 5–300 K using a Sumitomo RP-082E2S closed helium cycle cryostat. Temperature control and stabilization were performed using a Lake Shore Model 335 dual-channel temperature controller. Transmission spectra were recorded in unpolarized light ($\mathbf{k} \perp \mathbf{c}$), π ($\mathbf{k} \perp \mathbf{c}$, $\mathbf{E} \parallel \mathbf{c}$) and σ ($\mathbf{k} \perp \mathbf{c}$, $\mathbf{E} \perp \mathbf{c}$) polarizations. The spectral resolution was 0.05 cm^{−1} when recording spectra in unpolarized light and 0.3 cm^{−1} in π and σ polarizations. A KRS-5-based polarizer was used for the infrared region, and a film polarizer was used for the visible region.

To determine the *g* factors, the splittings of spectral lines corresponding to singlet-doublet transitions in a magnetic field were measured. The magnetic field parallel to the crystal's *c* axis was generated by permanent neodymium-iron-boron magnets placed in a cryostat next to the sample. The field strength, $B = 0.595 \pm 0.06$ T, was measured using a Hall magnetometer.

III. EXPERIMENTAL RESULTS

A. Energies, symmetries, and *g* factors for the crystal-field levels of Pr³⁺ in YAB:Pr³⁺

The wave functions of the CF levels of the Pr³⁺ ion, occupying a position with point symmetry group D_3 in YAB, are transformed according to two non-degenerate irreducible representations Γ_1 and Γ_2 and one doubly degenerate Γ_3 . The analysis of the temperature-dependent polarized absorption spectra of the YAB:Pr³⁺(1 at. %) crystal, with the use of selection rules, allowed us to determine energies and symmetries (irreducible representations) of 43 CF levels of Pr³⁺ in YAl₃(BO₃)₄:Pr³⁺ [41]. These data are given in Table I together with the data for the isostructural compound PrFe₃(BO₃)₄.

TABLE I. Energies E (cm⁻¹) of the CF levels of Pr³⁺ in YAl₃(BO₃)₄:Pr³⁺, experimentally found and calculated. Irreducible representations Γ and calculated g factors g_{\parallel} are also presented. Last two columns show the experimental data on the isostructural PrFe₃(BO₃)₄.

$^{2S+1}L_J$	i	Exp. YAB-Pr [41] E, Γ	Theory YAB-Pr This work			PrFe ₃ (BO ₃) ₄ [45]	
			E	Γ	g_{\parallel}	E	Γ
³ H ₄	1	0 Γ_2	0	Γ_2	0	0	Γ_2
	2	23 Γ_1	23	Γ_1	0	48.5	Γ_1
	3	226 Γ_3	225	Γ_3	1.80	192	Γ_3
	4	255	248	Γ_3	0.88	275	Γ_3
	5	493-635	493	Γ_3	2.34	500	Γ_3
	6	493-635	531	Γ_1	0	560	Γ_1
³ H ₅	A	2196 Γ_3	2189	Γ_3	7.481	2182.3	Γ_3
	B	2272	2274	Γ_2	0	2275.2	Γ_1
	C	-	2278	Γ_1	0	2295.5	Γ_2
	D	-	2329	Γ_3	7.45	2306.6	Γ_3
	E	-	2491	Γ_3	6.26	--	Γ_3
	F	-	2551	Γ_3	1.22	2588	Γ_3
	G	-	2613	Γ_2	0	--	Γ_2
³ H ₆	A	4295.5 Γ_3	4307	Γ_3	10.48	4292	Γ_3
	B	4338.7 Γ_3	4364	Γ_3	8.33	4355.2	Γ_3
	C	-	4491	Γ_2	0	--	Γ_2
	D	-	4511	Γ_1	0	4503.5	Γ_1
	E	-	4662	Γ_2	0	--	Γ_2
	F	4707 Γ_1	4673	Γ_1	0	4641	Γ_1
	G	4727.8 Γ_3	4693	Γ_3	3.19	4748	Γ_3
	H	4817.8 Γ_3	4788	Γ_3	1.60	4819.3	Γ_3
	I	4845 Γ_1	4808	Γ_1	0	4850	Γ_1
³ F ₂	A	5103 Γ_3	5111	Γ_3	0.08	5079	Γ_3
	B	5187 Γ_1	5147	Γ_1	0	5141.5	Γ_1
	C	5206 Γ_3	5188	Γ_3	2.57	5190.6	Γ_3
³ F ₃	A	6484.3 Γ_2	6492	Γ_3	0.72	6471.1	Γ_3
	B	6498.6 Γ_3	6497	Γ_2	0	6482.5	Γ_2
	C	6524	6534	Γ_3	3.60	6508	Γ_3
	D	6583.8 Γ_1	6566	Γ_2	0	6555	Γ_2
	E	6589.8 Γ_2	6581	Γ_1	0	6571.7	Γ_1
³ F ₄	A	6855.5 Γ_1	6852	Γ_1	0	6863	Γ_1
	B	6891.3 Γ_3	6888	Γ_3	1.64	6885.8	Γ_3
	C	6930 Γ_2	6936	Γ_2	0	6957.3	Γ_2
	D	6965 Γ_3	6972	Γ_3	3.47	6957.5	Γ_3
	E	-	7123	Γ_1	0	7099.5	Γ_1

	F	7150	7138	Γ_3	6.59	7107.8	Γ_3
1G_4	A	9707.4	9706	Γ_1	0	9728.5	Γ_1
	B	-	9774	Γ_3	0.94	9776.7	Γ_3
	C	9909 Γ_2	9909	Γ_2	0	9925.6	Γ_3
	D	10178	9946	Γ_3	3.16	9946	Γ_2
	E	10216	10261	Γ_3	5.63	10113.8	Γ_3
	F	-	10289	Γ_1	0	10193.4	Γ_1
1D_2	A	16512 Γ_1	16571	Γ_1	0	16491	Γ_1
	B	16754 Γ_3	16798	Γ_3	1.81	16791	Γ_3
	C	17140 Γ_3	17088	Γ_3	0.20	17080	Γ_3
3P_0	A	20603 Γ_1	20596	Γ_1	0	20567	Γ_1
$^3P_1 +$ 1I_6	A	21003 Γ_2	20952	Γ_2	0	20848	Γ_2
	B	21014 Γ_1	20959	Γ_1	0	20856	Γ_1
	C	21163 Γ_3	21171	Γ_3	3.07	21100	Γ_3
	D	-	21282	Γ_2	0	21280	Γ_2
	E	21330 Γ_1	21346	Γ_1	0	21382	Γ_3
	F	21353 Γ_3	21363	Γ_3	0.02	21420	Γ_1
	G	-	21409	Γ_3	0.18	21453	Γ_3
	H	-	21704	Γ_2	0	--	Γ_2
	I	-	21745	Γ_3	4.96	--	Γ_3
	K	21816 Γ_1	21764	Γ_1	0	21760	Γ_1
	L	21858.6 Γ_3	21819	Γ_3	6.43	21810	Γ_3
	A	22261 Γ_1	22260	Γ_1	0	22193	Γ_1
3P_2	B	22367 Γ_3	22358	Γ_3	0.96	22334	Γ_3
	C	22450 Γ_3	22442	Γ_3	4.87	--	Γ_3
1S_0	A	-	45968	Γ_1	0	-	-

In order to obtain additional information on the wave functions of the Γ_3 doublets, the transmission spectra of the YAB:Pr³⁺(1 at. %) sample were measured in a constant magnetic field $B = 0.595 \pm 0.06$ T, parallel to the c axis, at a temperature of 5 K. It was possible to measure the Zeeman splittings ΔE only for the three narrowest lines of the singlet-doublet transitions from the ground singlet to the doublets. They are listed in Table II together with g factors calculated as $g_{\parallel} = \Delta E/\mu_B B$. In the last column of Table II, the values calculated using wave functions obtained from CF calculations are presented

TABLE II. Measured splittings ΔE (cm^{-1}) of singlet-doublet optical transitions in magnetic field $\mathbf{B} \parallel \mathbf{c}$ and corresponding g factors $g_{\parallel} = \Delta E/\mu_B B$. The last column gives the calculated values of g_{\parallel} .

Transition	$\Delta E, \text{cm}^{-1}$	g_{\parallel}	$g_{\parallel, \text{theory}}$
$1\Gamma_2(^3\text{H}_4) \Rightarrow \text{A}\Gamma_3(^3\text{H}_5)$	2.2 ± 0.1	7.92 ± 1.15	7.48
$1\Gamma_2(^3\text{H}_4) \Rightarrow \text{A}\Gamma_3(^3\text{H}_6)$	2.8 ± 0.1	10.1 ± 1.37	10.48
$1\Gamma_2(^3\text{H}_4) \Rightarrow \text{B}\Gamma_3(^3\text{H}_6)$	2.5 ± 0.1	9 ± 1.26	8.335

B. Doublet structure of singlet-doublet transition lines

Figure 1 shows the absorption line corresponding to the singlet-doublet transition $1\Gamma_2(^3\text{H}_4) \rightarrow \text{B}\Gamma_3(^3\text{H}_6)$ in YAB:Pr³⁺ crystals with two different concentrations of praseodymium ions. The doublet structure is clearly visible, and the distance between the doublet components is noticeably greater in the spectrum of the crystal with a higher praseodymium concentration.

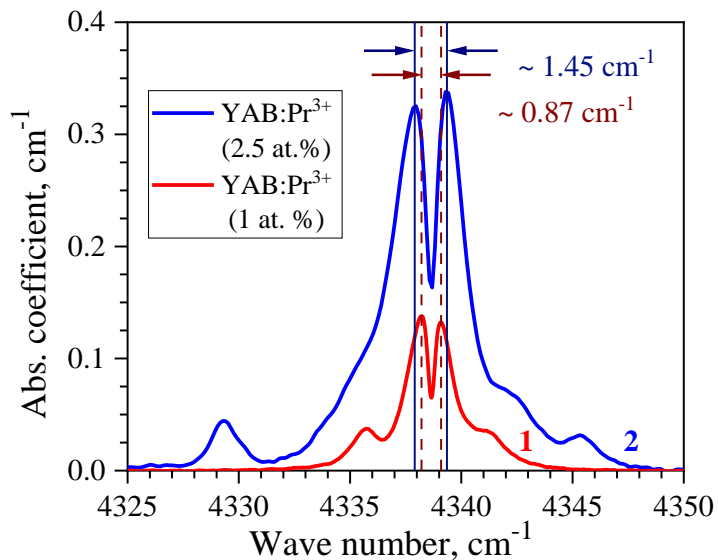


FIG. 1. Spectral absorption line of σ -polarized light corresponding to the transition $1\Gamma_2(^3\text{H}_4) \rightarrow \text{B}\Gamma_3(^3\text{H}_6)$ at $T=5$ K in YAB:Pr³⁺ crystals with a praseodymium ion concentration of 1 at.% (red curve 1) and 2.5% (blue curve 2).

Praseodymium is a monoisotopic element with one stable isotope, ¹⁴¹Pr, with a nuclear spin of $I = 5/2$. As a result of hyperfine interactions, the non-Kramers Γ_3 doublets are split into six hyperfine components. No hyperfine structure was detected in the recorded spectra. However, the a doublet structure of some spectral lines related to the singlet-doublet transitions $1\Gamma_2(^3\text{H}_4) \rightarrow \Gamma_3$ was observed (see Figs. 1 and 2). Such characteristic doublet line shape indicates the presence of random low-symmetry local perturbations of the crystal field, which can be caused by point defects of the crystal lattice [46].

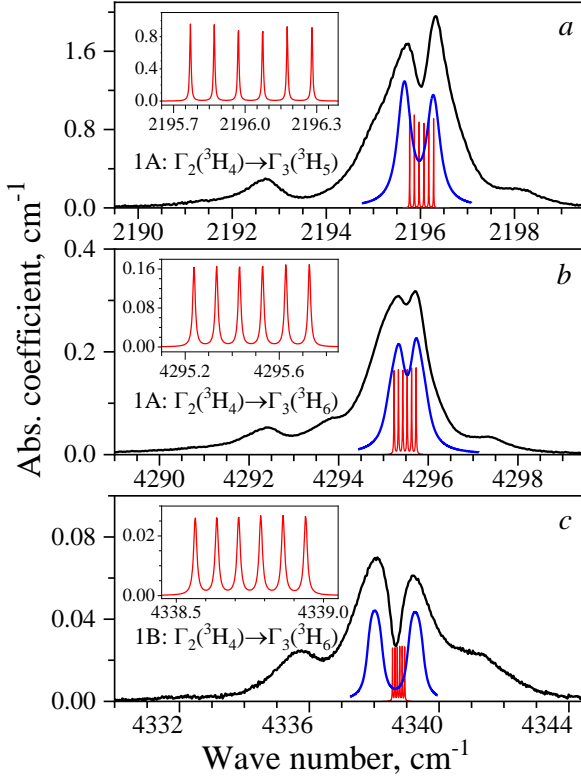


FIG. 2. Spectral absorption lines of unpolarized light related to the $\Gamma_2 \rightarrow \Gamma_3$ transitions in the YAB:Pr³⁺(1 at. %) crystal at $T=5$ K. The black line is the experiment, the red line is the calculated six-component hyperfine structure, the blue line is the calculated envelope of the hyperfine transitions from the ground singlet in the field of random lattice deformations under the assumption of a Lorentzian line shape of individual transitions with a half-width of 0.053 cm⁻¹.

Table III compares the observed splittings in the spectra of three different YAB:Pr³⁺ crystals. In crystals with 1 at. % praseodymium concentrations, grown with very different fluxes, the deformation splittings $\Delta(1\%)$ are identical, whereas in YAB:Pr³⁺(2.5 at. %) this splitting $\Delta(2.5\%)$ is significantly larger. The line intensity ratio confirms that the concentration ratio of praseodymium in these crystals is 2.5. (see Fig. 1). At the same time, the ratio of the observed splittings is noticeably smaller than 2.5. In [47,48], it was shown that during crystal growth using the solution-melt method, flux components enter the crystal. Mo³⁺ ions replace Al³⁺ ions, and Bi³⁺ takes the place of Y³⁺, creating additional defects [47]. Apparently, these defects as well as some other intrinsic defects of the crystal (e.g., vacancies), contribute to the deformation-induced splitting of RE³⁺ spectral lines in YAB:RE³⁺ crystals. At low concentration of defects, it is natural to assume an additivity of contributions from different kinds of defects and proportionality of each contribution to the concentration and the defect strength [46] and to present the deformation splittings as $\Delta(x\%) = \beta x + \Delta_i$. Here, β is a coefficient proportional to the defect strength $\Omega_{\text{Pr}} \sim [r(\text{Pr}^{3+}) - r(\text{Y}^{3+})]$ and Δ_i is the contribution from intrinsic defects. Assuming that Δ_i does not depend on the flux used (which was confirmed for the two studied YAB:Pr³⁺(1 at.%) crystals) and using the experimental data from Table III for the deformation splitting of the B $\Gamma_3(^3\text{H}_6)$ doublet in

crystals with a praseodymium concentration of 1 at.% and 2.5% (see Fig. 1), we obtain $\Delta_i = 0.48 \pm 0.07 \text{ cm}^{-1}$ for the contribution to the splitting caused by intrinsic defects.

TABLE III. Observed deformation splittings Δ of several lines of singlet-doublet transitions in different YAB:Pr crystals grown with different fluxes (indicated in the Table).

Optical transition	Frequency (cm^{-1})	Δ (cm^{-1})		
		YAB:Pr(1%) $\text{Bi}_2\text{Mo}_3\text{O}_{12}$	YAB:Pr(2.5%) $\text{K}_2\text{Mo}_3\text{O}_{10}$	YAB:Pr(1%) $\text{K}_2\text{O}/\text{MoO}_3/\text{B}_2\text{O}_3$
$1\Gamma_2(^3\text{H}_4) \rightarrow A\Gamma_3(^3\text{H}_5)$	2196	0.52 ± 0.03	0.71 ± 0.03	0.55 ± 0.02
$1\Gamma_2(^3\text{H}_4) \rightarrow A\Gamma_3(^3\text{H}_6)$	4295.5	0.34 ± 0.03	0.53 ± 0.03	0.39 ± 0.04
$1\Gamma_2(^3\text{H}_4) \rightarrow B\Gamma_3(^3\text{H}_6)$	4338.7	0.87 ± 0.03	1.45 ± 0.03	0.94 ± 0.05

IV. SIMULATION OF THE ABSORPTION SPECTRA

A. Crystal-field parameters for the Pr^{3+} ion in $\text{YAl}_3(\text{BO}_3)_4:\text{Pr}^{3+}$

The simulation of the absorption spectra of the $\text{YAl}_3(\text{BO}_3)_4$ crystal activated by Pr^{3+} ions, which replace Y^{3+} ions at the sites of the crystal lattice with local symmetry D_3 , was performed on the basis of calculations of the energy levels and the corresponding wave functions of the impurity ion by the method of successive numerical diagonalization of the Hamiltonian defined in the full space of electron-nuclear states of the ground electron configuration $4f^2$ with the dimension $D=C_{14}^2(2I+1)=546$ ($I=5/2$ is the nuclear spin of the only stable isotope of praseodymium ^{141}Pr),

$$H = H_0 + H_{\text{CF}} + H_Z + H_{\text{HFM}} + H_{\text{HFQ}} + H_{\text{el-def}}. \quad (1)$$

In operator (1), the first term,

$$H_0 = \zeta \sum_j \mathbf{l}_j \mathbf{s}_j + \alpha \hat{\mathbf{L}}^2 + \beta \hat{G}(G_2) + \gamma \hat{G}(R_7) + \sum_q (F^q \hat{f}_q + P^q \hat{p}_q + M^q \hat{m}_q), \quad (2)$$

presented in standard form [49], includes the energies of electrostatic interaction between $4f$ electrons, spin-orbit interaction (\mathbf{l}_j and \mathbf{s}_j are the orbital and spin moments of the j -th electron, respectively, $j=1,2$), additional contributions due to mixing of the ground and excited configurations, and relativistic interactions. The second term in (1) defines the energy of $4f$ electrons in the crystal field:

$$\begin{aligned} H_{\text{CF}} = & \sum_{j=1,2} \{ B_0^2 C_0^{(2)}(j) + B_0^4 C_0^{(4)}(j) + B_0^6 C_0^{(6)}(j) + i B_{-3}^4 [C_{-3}^{(4)}(j) + C_3^{(4)}(j)] \\ & + i B_{-3}^6 [C_{-3}^{(6)}(j) + C_3^{(6)}(j)] + B_6^6 [C_{-6}^{(6)}(j) + C_6^{(6)}(j)] \}. \end{aligned} \quad (3)$$

Here $C_q^{(p)}$ are spherical tensor operators of rank p , written in a Cartesian coordinate system with the z axis along the trigonal axis of symmetry c and the x axis along one of the C_2 axes in the ab plane; B_p^q are the crystal-field parameters calculated within the framework of the semi-phenomenological exchange-charge model [50]. This model takes into account the effects caused by the overlap of the wave functions of $4f$ electrons with the wave functions of electrons localised on the nearest lattice ions. Summing the contributions of the electrostatic fields of point charges of ions ($B_{q,el}^p$) and exchange charges on Pr^{3+} - O^{2-} bonds ($B_{q,ex}^p$), we obtain

$$B_q^{p;} = B_{q,el}^p + B_{q,ex}^p, \quad (4)$$

$$B_{q,el}^p = -K_p^q (1 - \sigma_p) e^2 \langle r^p \rangle \sum_{L,s} \frac{q_s}{R_{Ls}} V_p^q(\theta_{Ls}, \varphi_{Ls}), \quad (5)$$

$$B_{q,ex}^p = \frac{2(2p+1)}{7} K_p^q e^2 \sum_{\nu} [G_s S_s^2(R_{\nu}) + G_{\sigma} S_{\sigma}^2(R_{\nu}) + \gamma_p G_{\pi} S_{\pi}^2(R_{\nu})] \frac{V_p^q(\theta_{\nu}, \varphi_{\nu})}{R_{\nu}}, \quad (6)$$

where K_p^q are numerical coefficients [50], σ_p are screening factors [51], e is electron charge, $\langle r^p \rangle$ are moments of order p of the radial-distribution density of $4f$ electrons [52], $(-eq_s)$ is the charge of an s-type ion in the unit cell L of a crystal lattice with spherical coordinates R_{Ls}, θ_{Ls} and φ_{Ls} (the origin of the coordinate system is located on the RE ion under consideration). The functions of the angular coordinates of the lattice ions V_p^q are linear combinations of spherical functions [50]. In expression (6), the summation is carried out over the nearest neighbors of the RE ion, i.e., ligands ν at distances $R_{\nu} < 0.3$ nm. The overlap integrals of $4f$ wave functions of the RE ion $|n=4,l,m\rangle$ ($l=3, m=l_z$, the quantization axis z is directed along the vector \mathbf{R}_{ν}) with the wave functions of electrons on the filled ns ($l=0$), np ($l=1$) shells of oxygen ions $S_s(R_{\nu}) = \langle 4,3,0|n,0,0 \rangle$, $S_{\sigma}(R_{\nu}) = \langle 4,3,0|n,1,0 \rangle$, $S_{\pi}(R_{\nu}) = \langle 4,3,1|n,1,1 \rangle$ are calculated using the corresponding radial Hartree-Fock wave functions presented in the literature [52,53]; $\gamma_2=3/2$, $\gamma_4=1/3$, $\gamma_6=-3/2$ [50], G_s , G_{σ} and G_{π} are variable parameters of the model, determined from the analysis of experimental data on CF levels of the RE ion.

The interaction energy of $4f$ electrons with an external magnetic field \mathbf{B} is determined by the operator $H_Z = -\mathbf{M} \cdot \mathbf{B}$, where $\mathbf{M} = -\mu_B(k\mathbf{L} + 2\mathbf{S})$ is the operator of the magnetic moment of the RE ion, μ_B is the Bohr magneton, and k is the reduction factor of the orbital moment.

The operators of hyperfine magnetic dipole (H_{HFM}) and electric quadrupole (H_{HFQ}) interactions have the following form [54]:

$$H_{\text{HFM}} = A_{\text{HF}} \sum_j \{ \mathbf{I} \mathbf{l}_j + \frac{1}{2} [O_{2,j}^0 (3s_{z,j} I_z - s_j \mathbf{I}) + 3O_{2,j}^2 (s_{x,j} I_x - s_{y,j} I_y) + 3O_{2,j}^{-2} (s_{x,j} I_y + s_{y,j} I_x) + 6O_{2,j}^1 (s_{x,j} I_z + s_{z,j} I_x) + 6O_{2,j}^{-1} (s_{z,j} I_y + s_{y,j} I_z)] \}, \quad (7)$$

$$H_{\text{HFQ}} = \frac{e^2 Q(1 - \gamma_\infty)}{4I(2I - 1)} \sum_L q_L \frac{3z_L^2 - r_L^2}{r_L^5} I_0 - \frac{e^2 Q(1 - R_Q)}{4I(2I - 1)} \left\langle \frac{1}{r^3} \right\rangle_{4f} \sum_j [O_{2,j}^0 I_0 + 3O_{2,j}^2 I_2 + 3O_{2,j}^{-2} I_{-2} + 6O_{2,j}^1 I_1 + 6O_{2,j}^{-1} I_{-1}]. \quad (8)$$

Here, O_p^q are linear combinations of spherical tensor operators $C_q^{(p)}$, which coincide with the Stevens operators in the space of eigenfunctions of the angular momentum operator [55], $A_{\text{HF}} = 2\mu_B\gamma 3_{4f_{Pr}}$ is the magnetic hyperfine interaction constant, $\gamma_{Pr} = 2\pi \cdot 13.05 \text{ MHz/T}$ is the nuclear gyromagnetic ratio, $Q = -5.9 \cdot 10^{-30} \text{ m}^2$ is the quadrupole moment of the nucleus, $R_Q = 0.1$ and $\gamma_\infty = 80$ are the Sternheimer screening and anti-screening factors [56,57], and $\langle r^{-3} \rangle_{4f} = 5$ at. u. [58]. The matrices of operators $\sum_j O_{2,j}^q s_{\alpha,j}$ were constructed in the full basis of Slater determinants of the electron configuration $4f^2$. The first term in (8) determines the interaction of the quadrupole moment of the nucleus with the gradient of the electric field of the ionic lattice in the coordinate system centered on the praseodymium ion under consideration (\mathbf{r}_L is the radius vector of the ion with charge eq_L), the second term corresponds to the interaction with the electron shell, $I_0 = 3I_z^2 - I(I+1)$, $I_2 = I_x^2 - I_y^2$, $I_{-2} = I_x I_y + I_y I_x$, $I_1 = I_x I_z + I_z I_x$, $I_{-1} = I_y I_z + I_z I_y$.

The parameters of the Hamilton operator of a free ion (2) and the initial values of the CF parameters (see columns 1, 2, 4 in Table IV) were obtained from calculations of the energies of CF levels of Pr^{3+} ions with varying charges of ions in the yttrium, aluminum, boron, and oxygen sublattices and the parameters G_s , G_σ , G_π of the exchange-charge model to minimize deviations of the calculated energies from the measured ones. Results of variation: $q_Y = 3$, $q_{\text{Al}} = 2.68$, $q_B = 1.815$, $q_{\text{O1}}(9e) = -1.15$, $q_{\text{O2}}(9e) = -1.9$, $q_{\text{O3}}(18f) = -1.525$, $G_s = 2$, $G_\sigma = 2$ and $G_\pi = 1$; differences in the effective charges of oxygen ions in the Wyckoff positions 9e and 18f are due to covalent bonds in the BO_3 complexes. The final values of the CF parameters (column 5 in Table IV) were obtained by an additional procedure of directly varying the B_q^p parameters, taking into account the local lattice deformation when replacing Y^{3+} ions with an ionic radius of 0.90 Å with Pr^{3+} ions with an ionic radius of 0.99 Å [59]. The energies and symmetries of CF levels and g factors of the Γ_3 doublets calculated using this set of CF parameters are given in Table I. The calculated g factors $g_{||} = 2 < +|M_z|+>/\mu_B$ of the doublets ($|\pm>$ are the doublet wave functions), the Zeeman splittings of which were observed in the transmission spectra in an external magnetic field, are in satisfactory agreement with the measurement data (see Table II).

TABLE IV. Parameters of operators (2) and (3) (cm⁻¹).

Free-ion parameters Pr ³⁺ :YAl ₃ (BO ₃) ₄		Crystal-field parameters				
		Pr ³⁺ :YAl ₃ (BO ₃) ₄			PrFe ₃ (BO ₃) ₄	
1	2	3	4	5	6 [43]	7 [45]
$\zeta = 755.7$	$P^2=275$	$B_0^2=$	433	372	548±33	556
$F^2=67778$	$P^4=206$	$B_0^4=$	-1784	-1436	165±70	-1447
$F^4=49603$	$P^6=138$	$B_0^6=$	540	514	362±92	534
$F^6=32313$	$M^0=1.76$	$B_{-3}^4=$	1065	925	1336±49	867
$\alpha = 21.1$	$M^2=0.986$	$B_{-3}^6=$	127	195	457±67	165
$\beta = -665$	$M^4=0.546$	$B_6^6=$	287	377	-243±81	376
$\gamma = 1634$						

The CF parameters obtained in the present work (column 5 in Table IV) differ significantly from the corresponding parameters presented earlier in the literature (column 6 in Table IV), but are consistent with the parameters obtained in [45] (column 7 in Table IV) for the isostructural magnetically concentrated crystal PrFe₃(BO₃)₄CF. The agreement between the calculated energies of the CF levels and the experimental data has been noticeably improved. A number of contradictions between the arrangement of levels of different symmetries close in energy and a significantly underestimated total splitting of the ¹D₂ multiplet are due to neglect of mixing the ground electron configuration 4f² with excited ones (4f6p, 4f6s, see [45]) in simulating the optical spectrum.

B. Profiles of singlet-doublet transition lines

The Hamiltonian of the electron-deformation interaction has the following form:

$$H_{\text{el-def}} = \sum_{\Gamma=A,E} \sum_{k\lambda} V(\Gamma^k, \lambda) e(\Gamma^k, \lambda), \quad (9)$$

where the operators $V(\Gamma^k, \lambda)$ are defined by 30 independent parameters $b_p^q(\Gamma^k, \lambda)$,

$$V(\Gamma^k, \lambda) = \sum_{p,q} b_p^q(\Gamma^k, \lambda) O_p^q, \quad (10)$$

and $e(\Gamma^k, \lambda)$ are linear combinations of deformation tensor components $e_{\alpha\beta}$ (in the Cartesian coordinate system introduced above), transformed according to the irreducible representations A and E of the symmetry group D_3 ,

$$e(A^1) = (e_{xx} + e_{yy} + e_{zz})/\sqrt{3}, \quad e(A^2) = (2e_{zz} - e_{xx} - e_{yy})/\sqrt{12}, \quad (11)$$

$$e(E^1,1)=e_{xy}, \quad e(E^1,2)=(e_{xx} - e_{yy})/2, \quad e(E^2,1)=e_{xz}, \quad e(E^2,2)=e_{yz}, \quad (12)$$

The values of the parameters $b_p^q(\Gamma^k, \lambda)$ calculated within the framework of the exchange charge model [50] are given in Table V. The parameters of interaction with deformations $E^k,1$ and $E^k,2$ are related by the relations $b_p^q(E^k, 1) = b_p^{-q}(E^k, 2)$, if $q=1,2$, and $b_p^q(E^k, 1) = -b_p^{-q}(E^k, 2)$, if $q=4,5$.

TABLE V. Parameters of electron-deformation interaction (cm^{-1}) in the $\text{PrAl}_3(\text{BO}_3)_4$ crystal.

p	q	$b_p^q(A^1)$	$b_p^q(A^2)$	p	q	$b_p^q(E^1, 1)$	$b_p^q(E^2, 1)$
2	0	-262	1241	2	1	-4323	-4986
4	0	380	-87	4	1	204.3	1075
6	0	-74.9	-95.1	6	1	342.4	466
4	-3	-4721	-23.2	6	5	-281.5	-4389
6	-3	-644	838	2	-2	-1.5	-2165
6	6	-538	-333	4	-2	-790	429
				6	-2	34.3	348
				4	-4	976.5	-368
				6	-4	955.5	-211

Assuming a Lorentzian line shape for individual transitions between the hyperfine components of the sublevels Γ and Γ' of two multiplets, the intensity distribution of magnetic dipole absorption at the transition $\Gamma \rightarrow \Gamma'$ at temperature T (the profile of the hyperfine structure envelope) can be described by the formula

$$I(\Gamma \rightarrow \Gamma', E) = \sum_{j \in \Gamma} \sum_{k \in \Gamma'} \sum_{\alpha=x,y,z} | < j | M_{\alpha} | k > |^2 \exp[-(E_k - E_0)/k_B T] [(E_k - E_j - E)^2 + \Delta_{\Gamma\Gamma'}^2]^{-1}, \quad (13)$$

where $\Delta_{\Gamma\Gamma'}$ is the half-width of the spectral line of the electron-nuclear transition, E_0 is the energy of the lower hyperfine sublevel of the electron level Γ , and M is the effective dipole moment (electric or magnetic) of the transition under consideration.

In Fig. 3, the calculated six-component hyperfine structures of the lines corresponding to transitions from the ground singlet to the lower doublets in the $^3\text{H}_5$ and $^3\text{H}_6$ multiplets are compared with the observed profiles of these lines, which contain two broad overlapping components. The width of the dip at the center of the observed lines is significantly larger than the hyperfine structure intervals. We attribute the strong broadening and formation of the doublet structure to the interaction of the RE ions with the field of random deformations induced by both praseodymium impurity ions and intrinsic lattice point defects (molybdenum and bismuth ions in the aluminum and yttrium positions, respectively).

The distribution function of random deformations induced by point defects in an elastically anisotropic trigonal crystal lattice has the form [60]

$$g(e) = \frac{15\xi v_A}{8\pi^3 \gamma_A^2 \gamma_{E^1}^2 \gamma_{E^2}^2} \{ [v_A^2 e(A^1)^2 + e(A^2)^2] / \gamma_A^2 + [e(E^1, 1)^2 + e(E^1, 2)^2] / \gamma_{E^1}^2 + [e(E^2, 1)^2 + e(E^2, 2)^2] / \gamma_{E^2}^2 + \xi^2 \}^{-7/2}, \quad (14)$$

where the parameters $v_{\Gamma}, \gamma_{\Gamma}$ are determined by elastic constants and ξ is the distribution width proportional to the defect concentration and defect strength. In the calculations, the elastic constants of the $\text{HoAl}_3(\text{BO}_3)_4$ crystal [61] were used.

The spectral envelope of the singlet-doublet transition line is obtained by averaging the sum of the shape functions (13) of the hyperfine structure components over the distribution of random deformations (14):

$$I(\Gamma_2 \rightarrow \Gamma_3, E) \sim \int g(\mathbf{e}) \sum_m I_0(E - E_m(\mathbf{e})) d\mathbf{e}. \quad (15)$$

Here, E_m are the energies of the hyperfine sublevels of the doublet under consideration, equal to the corresponding eigenvalues of the Hamilton operator (1) for fixed components of the deformation tensor \mathbf{e} . We neglect the hyperfine structure of the Γ_2 singlet. As follows from the calculations performed, the dominant role in the splitting of the sextet hyperfine structure of electronic doublets into two triplets with an unresolved structure is played by shear deformations, transforming according to the irreducible representation E^2 . The calculated intensity distributions (15) of absorption lines at singlet-doublet transitions shown in Fig. 2 reproduce well the measurement data when using the width of the deformation distribution function $\xi = 7 \cdot 10^{-5}$ and the half-widths of the shape functions of electron-nuclear transitions $\Delta_{\Gamma\Gamma'} = 0.053 \text{ cm}^{-1}$.

The obtained value of ξ is significantly larger than $\xi \sim 10^{-6}$ found earlier from the simulation of lines' shape of singlet-doublet transitions in the spectra of $\text{LiLuF}_4:\text{Pr}^{3+}$ (0.1 at. %) [60] and $\text{RMO}_4:\text{Tm}^{3+}$ ($\text{R} = \text{Y, Lu}$, $\text{M} = \text{P, V}$; Tm concentrations 0.2 and 0.88 at. %) [46]. We note that a deformation splitting of 1.3 cm^{-1} for the first excited doublet in the ground multiplet of Tm^{3+} ions was observed in the THz spectra of $\text{TmAl}_3(\text{BO}_3)_4$ [62]. In this crystal grown by the solution-melt technique, Tm^{3+} ions are not an impurity but a part of a regular crystal structure, and the main defects are flux components entering the crystal during the growth process. The large width of the random deformation distribution function obtained from modelling the observed doublet deformation structure of singlet-doublet transitions in the spectra of YAB:Pr^{3+} indicates the possibility of strong correlations and attraction between intrinsic structural defects and praseodymium impurity ions in YAB:Pr^{3+} samples grown by the solution-melt method.

V. CONCLUSIONS

Transmission spectra of $\text{YAl}_3(\text{BO}_3)_4$ single crystals activated with Pr^{3+} ions at concentrations of 1 and 2.5 at.% were measured, including in a magnetic field parallel to the c axis of the crystal. The spectra were recorded in a wide spectral range ($2000\text{--}23,000 \text{ cm}^{-1}$) using high-resolution (up to 0.05 cm^{-1}) Fourier spectroscopy, which ensures high accuracy of the wave number scale. Pr^{3+} ions replace Y^{3+} ions in positions with point symmetry group D_3 . As a result of analysing temperature-dependent (5–300 K) spectra in π - and σ -polarised light, a diagram of CF levels of the Pr^{3+} ion in YAB:Pr^{3+} was constructed and irreducible representations of the point group D_3 (Γ_1 , Γ_2 , or Γ_3) were determined, according to which the wave functions of CF levels are transformed [41]. Measurements in a magnetic field allowed us to determine the g factors of several Γ_3 doublets. The spectra did not reveal any hyperfine structure caused by the interaction of

electrons with the magnetic moment of the nucleus of the only stable isotope of praseodymium, ^{141}Pr , with nuclear spin $I = 5/2$. However, for a number of singlet-doublet transition lines, a characteristic doublet structure was observed, caused by the action of random lattice deformations. Based on spectroscopic data, calculations were performed using crystal-field theory and the exchange-charge model. A physically justified set of crystal-field parameters was obtained. A calculation of the six-component hyperfine structure of Γ_3 doublets was performed. The calculated intervals of the hyperfine structure of doublets are significantly smaller than the deformation splitting observed in the spectra. The values of the electron-deformation interaction parameters were calculated within the framework of the exchange charge model. Using the previously obtained distribution function of random deformations induced by point defects in an elastically anisotropic trigonal crystal lattice, the profiles of deformation doublets observed in the optical spectrum were simulated. An estimate of the width of the random deformation distribution function has been obtained. Its large value may be due to a high concentration of impurities – flux components that enter the crystal during solution-melt growth.

ACKNOWLEDGEMENTS

The authors express their gratitude to N.Yu. Boldyrev for assistance in carrying out some of the measurements. The work was financially supported by the research projects FFUU-2024-0004 and FFUU-2025-0004 of the Institute of Spectroscopy of the Russian Academy of Sciences.

DATA AVAILABILITY

The data are available from the authors upon reasonable request.

References

- [1] E. V. Koporulina, N. I. Leonyuk, S. N. Barilo, L. A. Kurnevich, G. L. Bychkov, A. V. Mokhov, G. Bocelli, and L. Righi, Flux growth, composition, structural and thermal characteristics of $(\text{R}_x\text{Y}_{1-x})\text{Al}_3(\text{BO}_3)_4$ ($\text{R}=\text{Nd, Gd}$; $x=1, 0.6, 0.65, 0.7$ and 0.75) crystals, *J. Cryst. Growth.* **198**, 460 (1999). [https://doi.org/10.1016/S0022-0248\(98\)01228-7](https://doi.org/10.1016/S0022-0248(98)01228-7)
- [2] V. V. Maltsev, E. A. Volkova, D. D. Mitina, N. I. Leonyuk, A. B. Kozlov, and A. V. Shestakov, Growth and thermophysical properties of $\text{RAl}_3(\text{BO}_3)_4$ ($\text{R} = \text{Y, Nd, Gd, Lu}$) and $\text{RMgB}_5\text{O}_{10}$ ($\text{R} = \text{Y, La, Gd}$) crystals, *Inorg. Mater.* **56**, 612 (2020). <https://doi.org/10.1134/S0020168520060084>
- [3] S. Ilas, P. Loiseau, G. Aka, and T. Taira, 240 kW peak power at 266 nm in nonlinear $\text{YAl}_3(\text{BO}_3)_4$ single crystal, *Opt. Express* **22**, 30325 (2014). <https://doi.org/10.1364/OE.22.030325>
- [4] F. Cassouret, H. Robin, D. Balitski, S. Raissi, P. Loiseau, G. Aka, and T. Taira, in *Optica Laser Congress 2025, Technical Digest Series* (Optica Publishing Group, Prague, 2025), p. ATh3A.1. <https://opg.optica.org/abstract.cfm?URI=ASSL-2025-ATH3A.1>

[5] D. Jaque, Self-frequency-sum mixing in Nd doped nonlinear crystals for laser generation in the three fundamental colours: The NYAB case, *J. Alloys Compd.* **323–324**, 204 (2001). [https://doi.org/10.1016/S0925-8388\(01\)01111-2](https://doi.org/10.1016/S0925-8388(01)01111-2)

[6] D. Jaque, J. J. Romero, Continuous wave ultraviolet laser source based on self-frequency-sum-mixing in $\text{Nd}^{3+}:\text{YAl}_3(\text{BO}_3)_4$ nonlinear laser crystal, *J. Appl. Phys.* **90**, 1070 (2001). <https://doi.org/10.1063/1.1382828>

[7] P. Dekker, J. M. Dawes, and J. A. Piper, 2.27-W Q-switched self-doubling Yb:YAB laser with controllable pulse length, *JOSA B* **22**(2), 378 (2005). <https://doi.org/10.1364/JOSAB.22.000378>

[8] J. M. Dawes, P. Dekker, P. Burns, and J. A. Piper, Self-frequency-doubling ytterbium lasers, Optical review **12**, 101 (2005). <https://doi.org/10.1007/s10043-004-0101-8>

[9] N. I. Leonyuk and L. I. Leonyuk, Growth and characterization of $\text{RM}_3(\text{BO}_3)_4$ crystals, *Prog. Cryst. Growth Charact. Mater.*, **31**, 179 (1995). [https://doi.org/10.1016/0960-8974\(96\)83730-2](https://doi.org/10.1016/0960-8974(96)83730-2)

[10] E. Koporulina, N. I. Leonyuk, D. Hansen, and K. J. Bray, Flux growth and luminescence of $\text{Ho}:\text{YAl}_3(\text{BO}_3)_4$ and $\text{PrAl}_3(\text{BO}_3)_4$ crystals, *Cryst. Growth* **191**, 767 (1998). [https://doi.org/10.1016/S0022-0248\(98\)00347-9](https://doi.org/10.1016/S0022-0248(98)00347-9)

[11] E. Cavalli and N. I. Leonyuk, Comparative investigation on the emission properties of $\text{RAI}_3(\text{BO}_3)_4$ ($\text{R} = \text{Pr, Eu, Tb, Dy, Tm, Yb}$) crystals with the huntite structure, *Crystals* **9**, 44 (2019). <https://doi.org/10.3390/crust9010044>

[12] E. Bovero, Z. D. Luo, Y. D. Huang, A. Benayas, and D. Jaque, Single longitudinal mode laser oscillation from a neodymium aluminium borate stoichiometric crystal, *Appl. Phys. Lett.* **87**, 211108 (2005). <https://doi.org/10.1063/1.2133893>

[13] P. A. Burns, J. M. Dawes, P. Dekker, J. A. Piper, J. Li, J. Wang, Coupled-cavity, single-frequency, tunable cw Yb:YAB yellow microchip laser, *Optics Communications* **207**, 315 (2002). [https://doi.org/10.1016/S0030-4018\(02\)01500-6](https://doi.org/10.1016/S0030-4018(02)01500-6)

[14] B. Weichelt, M. Rumpel, A. Voss, A. Gross, V. Wesemann, D. Rytz, M. A. Ahmed, and T. Graf, Yb:YAl₃(BO₃)₄ as gain material in thin-disk oscillators: demonstration of 109 W of IR output power, *Opt. Express* **22**, 25708 (2013). <https://doi.org/10.1364/OE.21.025708>

[15] H.-J. Zeng, Z.-L. Lin, V. Petrov, P. Loiko, Y. Chen, Y. Huang, G. Zhang, X. Mateos, W.-Z. Xue, H. Lin, L. Wang, and W. Chen, 56-fs diode-pumped SESAM mode-locked Yb:YAl₃(BO₃)₄ laser, *Opt. Express* **31**, 10617 (2023). <https://doi.org/10.1364/OE.486577>

[16] R. P. Chaudhury, B. Lorenz, Y. Y. Sun, L. N. Bezmaternykh, V. L. Temerov, and C. W. Chu, Magnetoelectricity and magnetostriction due to the rare-earth moment in $\text{TmAl}_3(\text{BO}_3)_4$, *Phys. Rev. B* **81**, 220402R (2010). <https://doi.org/10.1103/PhysRevB.81.220402>

[17] K.-C. Liang, R. P. Chaudhury, B. Lorenz, Y. Y. Sun, L. N. Bezmaternykh, V. L. Temerov, and C. W. Chu, Giant magnetoelectric effect in $\text{HoAl}_3(\text{BO}_3)_4$, *Phys. Rev. B* **83**, 180417(R) (2011). <https://doi.org/10.1103/PhysRevB.83.180417>

[18] A. M. Kadomtseva, Yu. F. Popov, G. P. Vorob'ev, N. V. Kostyuchenko, A. I. Popov, A. A. Mukhin, V. Yu. Ivanov, L. N. Bezmaternykh, I. A. Gudim, V. L. Temerov, A. P. Pyatakov, and A. K. Zvezdin, High-temperature magnetoelectricity of terbium aluminum borate: the role of

excited states of the rare-earth ion, *Phys. Rev. B* **89**, 014418 (2014).

<https://doi.org/10.1103/PhysRevB.89.014418>

[19] N. V. Kostyuchenko, V. Y. Ivanov, A. A. Mukhin, A. I. Popov, and A. K. Zvezdin, Features of magnetic and magnetoelectric properties in rare-earth aluminum borates $\text{RAI}_3(\text{BO}_3)_4$, *IEEE Transactions on magnetics* **50**, 2504504 (2014). <https://doi.org/10.1109/TMAG.2014.2329954>

[20] H. S. Yoo, W. B. Im, J. H. Kang, and D. Y. Jeon, Preparation and photoluminescence properties of $\text{YAl}_3(\text{BO}_3)_4:\text{Tb}^{3+}, \text{Bi}^{3+}$ phosphor under VUV/UV excitation, *Opt. Mat.* **31**, 131 (2008). <https://doi.org/10.1016/j.optmat.2008.02.005>

[21] G. V. Lokeshwara Reddy, L. Rama Moorthy, T. Chennaiah, and B. C. Jamalaiah, Multi-color emission tunability and energy transfer studies of $\text{YAl}_3(\text{BO}_3)_4:\text{Eu}^{3+}/\text{Tb}^{3+}$ phosphors, *Ceramics International* **40**, 3399 (2014). <https://doi.org/10.1016/j.ceramint.2013.09.092>

[22] B. C. Jamalaiah, G. V. Reddy, and G. W. Lokeshwara, Blue emitting $\text{YAl}_3(\text{BO}_3)_4:\text{Tm}^{3+}$ single-phase phosphors under UV excitation, *Phys. Chem. Glasses: Eur. J. Glass Sci. Technol. B* **57**, 68 (2016). <https://doi.org/10.13036/17533562.57.2.008>

[23] D. Yu, H. Li, D. Zhang, Q. Zhang, A. Meijerink, and M. Suta, One ion to catch them all: targeted high-precision Boltzmann thermometry over a wide temperature range with Gd^{3+} , *Light Sci. Appl.* **10**, 236 (2021). <https://doi.org/10.1038/s41377-021-00677-5>

[24] A. M. El-Naggar, N. S. Alzayed, A. Majchrowski, L. Jaroszewicz, M. G. Brik, W. Kuznik, I. V. Kityk, Preparation and fluorescence properties of $\text{La}_2\text{CaB}_{10}\text{O}_{19}$ crystals doped with Pr^{3+} ions, *J. Cryst. Growth*, **334**, 122 (2011). <https://doi.org/10.1016/j.jcrysgro.2011.08.037>

[25] N. Navya, B. R. Radha Krushna, S. C. Sharma, N. R. Nadar, M. Panda, A. George, C. Krithika, S. Rajeswari, R. Vanithamani, K. Madhavi, G. Ramakrishna, K. Manjunatha, S. Y. Wu, H. Nagabhushana, Probing multifunctional applications of $\text{CeO}_2:\text{Pr}^{3+}$ phosphor for optical thermometry, flexible displays, cheiloscopy, anti-counterfeiting applications, *J. Photochem. Photobiol. A Chem.*, **456**, 115858 (2024). <https://doi.org/10.1016/j.jphotochem.2024.115858>

[26] N. Rebrova, A. Grippa, P. Zdeb, P. J. Deren, Blue to UV upconversion properties of Pr^{3+} doped ACaF_3 ($\text{A} = \text{K}, \text{Rb}, \text{Cs}$) phosphors, *Scripta Materialia* **255**, 116395 (2025). <https://doi.org/10.1016/j.scriptamat.2024.116395>

[27] Y. Hua, Yellow-emitting $\text{Ca}_2\text{Gd}(\text{Sb},\text{Nb})\text{O}_6:\text{Pr}^{3+}$ double-perovskite phosphors excitable by blue-green light, *Ceramics International* **50**, 32353 (2024). <https://doi.org/10.1016/j.ceramint.2024.06.043>

[28] T. Gün, P. Metz, G. Huber, Efficient continuous wave deep ultraviolet $\text{Pr}^{3+}:\text{LiYF}_4$ laser at 261.3 nm, *Appl. Phys. Lett.* **99**, 181103 (2011). <https://doi.org/10.1063/1.3657150>

[29] P. W. Metz, S. Müller, F. Reichert, D.-T. Marzahn, F. Moglia, C. Kränel, and G. Huber, Wide wavelength tunability and green laser operation of diode-pumped $\text{Pr}^{3+}:\text{KY}_3\text{F}_{10}$, *Opt. Express* **21**, 31274 (2013), <https://doi.org/10.1364/OE.21.031274>

[30] S. Fujita, H. Tanaka, and F. Kannari, Output characteristics of $\text{Pr}:\text{YAlO}_3$ and $\text{Pr}:\text{YAG}$ lasers pumped by high-power GaN laser diodes, *Appl. Opt.* **59**, 5124 (2020). <https://doi.org/10.1364/AO.394792>

[31] R. Fang, R. Huang, H. Xu, Z. Cai, and Y. Wang, Continuously tunable deep-red laser based on $\text{Pr}^{3+}:\text{YLF}$, *Opt. Laser Technol.* **164**, 109487 (2023). <https://doi.org/10.1016/j.optlastec.2023.109487>

[32] Z. Zhang, W. Yuan, R. Fang, Z. Li, H. Xu, and Z. Cai, Highly efficient LD-pumped high power 718.5 nm Pr^{3+} :YLF laser, *Opt. Com.* **566**, 130726 (2024)
<https://doi.org/10.1016/j.optcom.2024.130726>

[33] Y. Li, S. Jiang, L. Zhong, Y. Wang, B. Yang, Y. Wang, G. Xiang, X. Tang, F. Ling, L. Li, and X. Zhou, Ultra-sensitive low-temperature luminescent thermometry based on Boltzmann behavior of the Stark sub-levels of Pr^{3+} , *J. Alloys Compd.* **1009**, 176842 (2024).
<https://doi.org/10.1016/j.jallcom.2024.176842>.

[34] P. Goldner and O. Guillot-Noël, Magnetic interactions in Pr^{3+} : LiYF_4 for quantum manipulation: search for an efficient three-level Λ system, *Mol. Phys.* **102**, 1185 (2004).
<https://doi.org/10.1080/00268970410001728744>

[35] G. J. Pryde, M. J. Sellars, and N. B. Manson, Phase-dependent decoherence of optical transitions in Pr^{3+} : LaF_3 in the presence of a driving field, *Physical Review B* **69**, 075107 (2004).
<https://doi.org/10.1103/PhysRevB.69.075107>

[36] E. Fraval, M. J. Sellars, and J. J. Longdell, Method of extending hyperfine coherence times in Pr^{3+} : Y_2SiO_5 , *Phys. Rev. Lett.* **92**, 077601 (2004).
<https://doi.org/10.1103/PhysRevLett.92.077601>

[37] E. Fraval, M. J. Sellars, and J. J. Longdell, Dynamic decoherence control of a solid-state nuclear-quadrupole qubit, *Phys. Rev. Lett.* **95**, 030506 (2005).
<https://doi.org/10.1103/PhysRevLett.95.030506>

[38] J. J. Longdell, E. Fraval, M. J. Sellars, and N. B. Manson, Stopped light with storage times greater than one second using electromagnetically induced transparency in a solid, *Phys. Rev. Lett.* **95**, 063601 (2005). <https://doi.org/10.1103/PhysRevLett.95.063601>

[39] G. Heinze, C. Hubrich, and T. Halfmann, Coherence time extension in Pr^{3+} : Y_2SiO_5 by self-optimized magnetic fields and dynamical decoupling, *Physical Review A* **89**, 053825 (2014).
<https://doi.org/10.1103/PhysRevA.89.053825>

[40] O. Guillot-Noël, Ph. Goldner, Y. Le Du, and P. Loiseau, Hyperfine structure, optical dephasing, and spectral-hole lifetime of single-crystalline Pr^{3+} : $\text{La}_2(\text{WO}_4)_3$, *Physical Review B* **75**, 205110 (2007). <https://doi.org/10.1103/PhysRevB.75.205110>

[41] T.A. Igolkina, E. P. Chukalina, K. N. Boldyrev, I. A. Gudim, and M. N. Popova, High-resolution spectroscopy of $\text{YAl}_3(\text{BO}_3)_4$: Pr^{3+} , *Optics and Spectroscopy* **132**(11), 1110 (2024).
<https://journals.ioffe.ru/articles/60318> [Translated from: *Optika i Spektroskopya* **132**(11), 1175 (2024). <https://journals.ioffe.ru/articles/59507>]

[42] M. H. Bartl, K. Gatterer, E. Cavalli, A. Speghini, and M. Bettinelli, Growth, optical spectroscopy and crystal field investigation of $\text{YAl}_3(\text{BO}_3)_4$ single crystals doped with tripositive praseodymium, *Spectrochim. Acta A* **57**, 1981 (2001). [https://doi.org/10.1016/S1386-1425\(01\)00484-X](https://doi.org/10.1016/S1386-1425(01)00484-X)

[43] M. Mazzera, A. Baraldi, E. Buffagni, R. Capelletti, E. Beregi, I. Földvári, and N. Magnani, Spectroscopic analysis of Pr^{3+} crystal-field transitions in $\text{YAl}_3(\text{BO}_3)_4$, *Appl. Phys. B* **104**, 603 (2011). <https://doi.org/10.1007/s00340-011-4421-7>

[44] I. A. Gudim, E. V. Eremin, and V. L. Temerov, Flux growth and spin reorientation in trigonal $\text{Nd}_{1-x}\text{Dy}_x\text{Fe}_3(\text{BO}_3)_4$ single crystals, *J. Cryst. Growth* **312**(16-17), 2427 (2010). <https://doi.org/10.1016/j.jcrysgro.2010.05.013>

[45] M. N. Popova, T. N. Stanislavchuk, B. Z. Malkin, and L. N. Bezmaternykh, Optical spectroscopy of $\text{PrFe}_3(\text{BO}_3)_4$: Crystal-field and anisotropic Pr-Fe exchange interactions, *Phys. Rev. B Condens. Matter*, **80**(19), 195101 (2009). <https://doi.org/10.1103/PhysRevB.80.195101>

[46] B. Z. Malkin, N. M. Abishev, E. I. Baibekov, D. S. Pytalev, K. N. Boldirev, M. N. Popova, and M. Bettinelli, Distribution function of random strains in elastically anisotropic continuum and defect strengths of impurity Tm^{3+} ions in crystals with zircon structure, *Phys. Rev. B* **96**, 014116(1-13) (2017). <https://doi.org/10.1103/PhysRevB.96.014116>

[47] M. N. Popova, K. N. Boldyrev, P. O. Petit, B. Viana and L. N. Bezmaternykh, High-resolution spectroscopy of $\text{YbAl}_3(\text{BO}_3)_4$ stoichiometric nonlinear laser crystals, *J. Phys.: Condens. Matter* **20**, 455210 (2008).

[48] K. N. Boldyrev, M. N. Popova, M. Bettinelli, V. L. Temerov, I. A. Gudim, L. N. Bezmaternykh, P. Loiseau, G. Aka, and N. I. Leonyuk, *Opt. Mat.* **34**(11), 1885 (2012). <https://doi.org/10.1016/j.optmat.2012.05.021>

[49] W. T. Carnall, G. L. Goodman, K. Rajnak, and R.S. Rana, A systematic analysis of the spectra of the lanthanides doped into single crystal LaF_3 , *J. Chem. Phys.* **90**, 3443 (1989). <https://doi.org/10.1063/1.455853>

[50] B. Z. Malkin, Crystal field and electron-phonon interaction in rare-earth ionic paramagnets, *Mod. Probl. Condens. Matter* **21**, 13 (1987). <https://doi.org/10.1016/B978-0-444-87051-3.50008-0>

[51] R. P. Gupta and S. K. Sen, Sternheimer shielding-antishielding; rare-earth ions, *Phys. Rev. A* **7**, 850 (1973). <https://doi.org/10.1103/PhysRevA.7.850>

[52] A. J. Freeman and R. E. Watson, Theoretical investigation of some magnetic and spectroscopic properties of rare-earth ions, *Phys. Rev.* **127**, 2058 (1962)

[53] E. Clementi and A.D. McLean, Atomic negative ions, *Phys. Rev.* **133**, **419** (1964). <https://doi.org/10.1103/PhysRev.133.A419>

[54] D. S. Pytalev, E. P. Chukalina, M. N. Popova, G. S. Shakurov, S. L. Korabileva, and B. Z. Malkin, Hyperfine interactions of Ho^{3+} ions in KY_3F_{10} : electron paramagnetic resonance and optical spectroscopy studies, *Phys. Rev. B* **86**, 115124 (2012). <https://doi.org/10.1103/PhysRevB.86.115124>

[55] V. V. Klekovkina, A. R. Zakirov, B. Z. Malkin, and L. A. Kasatkina, *J. Phys.: Conf. Ser.* **324**, 012036 (2011). DOI: 10.1088/1742- 6596/324/1/012036

[56] M. A. H. McCausland and I. S. Mackenzie, Nuclear magnetic resonance in rare earth metals, *Adv. Phys.* **28**, 305 (1979). <https://doi.org/10.1080/00018737900101385>

[57] K. K. Sharma and L. E. Erickson, Optical and Zeeman studies of the f^4 configurations of Pr^{3+} in LaCl_3 and LaBr_3 , *J. Phys. C* **14**, 1329 (1981).

[58] A. Abragam and B. Bleaney, *Electron paramagnetic resonance of transition ions* (Oxford Univ. Press, Oxford. 1970).

[59] R. D. Shannon, Revised effective ionic radii and systematic studies of interatomic distances in halides and chalcogenides, *Acta Cryst. A* **32**, 751 (1976).

[60] N. M. Abishev, E. I. Baibekov, B. Z. Malkin, M. N. Popova, D. S. Pytalev, and S. A. Klimin, Deformation broadening and the fine structure of spectral lines in optical spectra of dielectric crystals containing rare-earth ions, *Physics of the Solid State*, **61**(5), 795 (2019). <https://doi.org/10.1134/S1063783419050020> [Fizika Tverdogo Tela **61**, 898 (2019)]. <https://doi.org/10.21883/FTT.2019.05.47589.22F>

[61] I. V. Bilych, M. P. Kolodyazhnaya, K. R. Zhekova, G. A. Zvyagina, V. D. Fil, and I. A. Gudim, Elastic, magnetoelastic, magnetopiezoelectric, and magnetodielectric characteristics of $\text{HoAl}_3(\text{BO}_3)_4$, *Low Temp. Phys.* **46**, 923 (2020). <https://doi.org/10.1063/10.0001715>

[62] A. M. Kuzmenko, A. A. Mukhin, V. Yu. Ivanov, G. A. Komandin, A. Shubaev, A. Pimenov, V. Dziom, L. N. Bezmaternykh, and I. A. Gudim, Terahertz spectroscopy of crystal-field transitions in magnetoelectric $\text{TmAl}_3(\text{BO}_3)_4$, *Phys. Rev. B* **94**, 174419 (2016). <https://doi.org/10.1103/PhysRevB.94.174419>